Journal of Physics:
Condensed Matter

PURPOSE-LED
PUBLISHING™

PAPER • **OPEN ACCESS**

Emergence of a metallic surface state for narrow bandgap Mott insulator $Sr_3Ir_2O_7$(001) thin films

To cite this article: Takashi Komesu *et al* 2025 *J. Phys.: Condens. Matter* **37** 175002

View the article online for updates and enhancements.

You may also like

- The anomalous temperature dependent low energy electron diffraction intensity at epitaxial $Sr_3Ir_2O_7$ thin film surfaces
  Peace Ikeoluwa Adegbite, Arjun Subedi, Yuanyuan Zhang et al.
- A review of progress in theoretical modeling of polarization dynamics in ferroelectric materials
  Haohua Wen, Jianyi Liu, Jinhong Li et al.
- Thermoelectric behavior of Ruddlesden–Popper series iridates
  I Pallecchi, M T Buscaglia, V Buscaglia et al.

This content was downloaded from IP address 129.93.161.216 on 16/09/2025 at 19:42

OPEN ACCESS
IOP Publishing
Journal of Physics: Condensed Matter
J. Phys.: Condens. Matter **37** (2025) 175002 (8pp)
https://doi.org/10.1088/1361-648X/adbecf

Emergence of a metallic surface state for narrow bandgap Mott insulator $Sr_3Ir_2O_7$(001) thin films

Takashi Komesu[1,*], **Yuanyuan Zhang**[1], **Shiv Kumar**[2], **Amit Kumar**[2], **Yudai Miyai**[3], **Kenya Shimada**[2,4,5], **Peace Ikeoluwa Adegbite**[1], **Xia Hong**[1] and **P A Dowben**[1,*]

[1] Department of Physics and Astronomy, Theodore Jorgensen Hall, University of Nebraska, 855 N 16th, Lincoln, NE 68588-0299, United States of America
[2] Research Institute for Synchrotron Radiation Science (HiSOR), Hiroshima University, Higashi-Hiroshima 739-0046, Japan
[3] Graduate School of Advanced Science and Engineering, Hiroshima University, Higashi-Hiroshima 739-8526, Japan
[4] The International Institute for Sustainability with Knotted Chiral Meta Matter (WPISKCM2), Hiroshima University, Higashi-Hiroshima 739-8526, Japan
[5] Research Institute for Semiconductor Engineering (RISE), Hiroshima University, Higashi-Hiroshima 739-8527, Japan

E-mail: tkomesu2@unl.edu and pdowben1@unl.edu

Received 3 January 2025, revised 3 March 2025
Accepted for publication 10 March 2025
Published 25 March 2025

Abstract

We report evidence of a finite density of states at the Fermi level at the surface of epitaxial thin films of the narrow bandgap Mott insulator $Sr_3Ir_2O_7$(001). The Brillouin zone critical points for $Sr_3Ir_2O_7$(001) thin films have been determined by a comparison of the band mapping from angle-resolved photoemission spectroscopy and low energy electron diffraction. Angle-resolved x-ray photoemission studies reveal the surface termination of $Sr_3Ir_2O_7$(001) is Sr–O. The absence of dispersion with photon energy, or changing wave vector along the surface normal, indicates the two-dimensional character of the bands contributing to the density of states close to the Fermi level for $Sr_3Ir_2O_7$(001) thin films. Thus, the finite density of states at the Fermi level is attributed to surface states or surface resonances. The appearance of a finite density of states at the Fermi level is consistent with the increased conductivity with decreasing film thickness for ultrathin $Sr_3Ir_2O_7$(001) films.

Supplementary material for this article is available online

Keywords: angle resolved photoemission spectroscopy, electronic structure, surface states

---

[*] Authors to whom any correspondence should be addressed.

Original content from this work may be used under the terms of the Creative Commons Attribution 4.0 licence. Any further distribution of this work must maintain attribution to the author(s) and the title of the work, journal citation and DOI.

© 2025 The Author(s). Published by IOP Publishing Ltd

1. Introduction

The Ruddlesden–Popper strontium iridates $Sr_{n+1}Ir_nO_{3n+1}$ series show a transition from Mott insulator to semimetal states with increasing n, which can be attributed to the increasing Ir coordination numbers [1, 2]. It has been shown that $Sr_3Ir_2O_7$ ($n = 2$) has an insulating ground state with vanishing bandgap [2–4], which makes its electronic state highly susceptible to small perturbations. Epitaxial thin films of strontium iridates $Sr_{n+1}Ir_nO_{3n+1}$ open the door to quantum confinement and symmetry breaking [5–7]. Furthermore, epitaxial strain imposed by the substrate can lead to changes in the electronic structure [1, 2, 6–11].

In this regard, it is also of interest to see if the band structure of $Sr_3Ir_2O_7(001)$ thin films resembles other strontium iridates thin films subjected to quantum confinements, as is suggested by a comparison of the many iridate band structures studied to date [1]. For example, the atomic arrangement of monolayer $SrIrO_3$ closely resembles the central regions of $Sr_3Ir_2O_7$ unit cell, while $SrIrO_3(001)$ exhibits a film-thickness-driven metal-insulator transition [9, 12, 13] and strain induced surface reconstructions [1, 12, 14]. The different experimental band structures of the bulk single crystals of $Sr_3Ir_2O_7(001)$ [15, 16] are not in full agreement. One angle-resolved photoemission (ARPES) study [15] showed that the surface of bulk single crystals of $Sr_3Ir_2O_7(001)$ exhibits a finite electronic spectral weight at the Fermi level, suggesting weak metallicity at the surface. Another experimental band structure mapping, by ARPES, revealed a small band gap less than 97 meV [16], consistent with the band gap extracted from the dI/dV curves obtained from scanning tunneling microscopy [17].

For $SrIrO_3(001)$, the surface is seen to be Sr-O terminated [14], which is also the case for $Sr_3Ir_2O_7$ single crystals [17]. The experimental band structure, obtained from the surface sensitive ARPES experiments, may be dominated by this surface layer, and thus decoupled from the bulk of the film, as noted for $SrIrO_3(001)$ [14].

2. Experimental methods

We deposited 4.2–19.8 nm, or 2–9.5 unit cells (u.c.), thick $Sr_3Ir_2O_7(001)$ (SIO327) thin films epitaxially on (001) $(LaAlO_3)_{0.3}(Sr_2TaAlO_6)_{0.7}$ (LSAT) substrates through off-axis radio frequency magnetron sputtering. The films were deposited at 630 °C, with 50 mTorr process gas composed of Ar and O_2 (ratio 40:1). After growth, the films were cooled down to room temperature in process gas. Atomic force microscopy measurements revealed a smooth surface morphology for these samples with root-mean-square roughness of 3 Å, as seen in supplementary figure S1. The x-ray diffraction θ–2θ scan shows that the $Sr_3Ir_2O_7(001)$ thin films are single crystalline without impurity phases. The c-axis lattice constant is 21.0 Å for the 6.5 u.c. (13.6 nm) thick $Sr_3Ir_2O_7(001)$ film, slightly larger than the bulk value (20.879 Å) [18–20]. The in-plane lattice parameters of the $(LaAlO_3)_{0.3}(Sr_2TaAlO_6)_{0.7}$ substrate (CrysTec. Inc) and bulk $Sr_3Ir_2O_7$ are 3.87 Å and 3.896 Å [19], respectively, imposing an in-plane compressive strain of -0.67% on the epitaxial $Sr_3Ir_2O_7$ thin films. The slightly expanded c-axis lattice constant is consistent with the compressive strain. The film thickness was determined by fitting to the Laue oscillations around the main Bragg peak (supplementary figure 1(c) inset). For comparison, we also examined a 12.5 u.c. (5 nm) $SrIrO_3(001)$ (SIO113) film on $SrTiO_3$ substrate. The growth conditions for the $SrIrO_3(001)$ (SIO113) film can be found in [13].

Angle-resolved x-ray photoemission spectroscopy measurements were carried out using an Al-Kα unmonochromatized SPECS x-ray source with photon energy of 1486.6 eV, and the energies of the emitted photoelectrons were analyzed with a VG100AX hemispherical analyzer. The x-ray spectroscopy of the Ir 4f and the Sr 3d core levels show well resolved spin-orbit splitting between the Ir $4f_{7/2}$ and Ir $4f_{5/2}$ (3.1 ± 0.1 eV)) and the Sr $3d_{5/2}$ and Sr $3d_{3/2}$ (1.6 eV), with no indications of surface hydride formation [21–23], as seen in the supplementary figure S2. The Ir $4f_{7/2}$ and Ir $4f_{5/2}$ core level binding energies are at 63.2 ± 0.1 eV and 66.3 ± 0.1 eV, respectively, as seen in the supplementary figure S2. These values are in good agreement with previously reported values of 63.5 eV ($4f_{7/2}$) and 66.4 eV ($4f_{5/2}$) [22], as well as 62.8 eV ($4f_{7/2}$) and 65.9 eV ($4f_{5/2}$) [24]. The Sr $3d_{5/2}$ core level binding energies at 132.9 ± 0.1 eV, as seen in figure S2, is in good agreement with the XPS core level binding energy values of 133 eV reported for SrO [25], 133.5 eV reported for $SrMoO_4$ [26], and 133 eV reported for $SrRh_2O_4$ [26].

The experimental electronic structure measurements were performed on several thicknesses of $Sr_3Ir_2O_7$ films using various spectroscopic methods. The ARPES studies were performed on the linear undulator beamline (BL-1) of the Research Institute for Synchrotron Radiation Science (HiSOR), Hiroshima University [27, 28]. The ARPES experiments were carried out using an angular (display) mode of the hemispherical electron analyzer (R4000, VG-Scienta) with an acceptance angle of ±15°. We used several different incident photon energies, focusing on results obtained at $h\nu$ between 50 and 150 eV. The energy resolution was limited by temperature, not the instrument, and estimated to be about 30 meV at room temperature. The angular resolution was ±0.1°, corresponding to a wave vector resolution of 0.01 ± 0.005 Å^{-1} for $h\nu = 71$ eV at the Fermi level (E_F). Throughout this work, the binding energies are referenced to the Fermi level ($E - E_F$) of an Au film electrically connected to the sample. We have measured ARPES in the p-polarization geometry, where the electric field vector lies in the plane of incidence as well as the photoelectron detection plane. $SrIrO_3(001)$ and $Sr_3Ir_2O_7(001)$ samples were treated with several successive annealing steps at ~560 °C with O_2 gas pressure of 8×10^{-8} Torr for about 30 min.

Low energy electron diffraction (LEED) images were taken *in situ* using an Omicron SPECTALEED rear-view LEED optics system with electron beam energy of 38.5 eV and other energies. Sample crystallographic conditions were seen to be very sensitive to surface preparation.

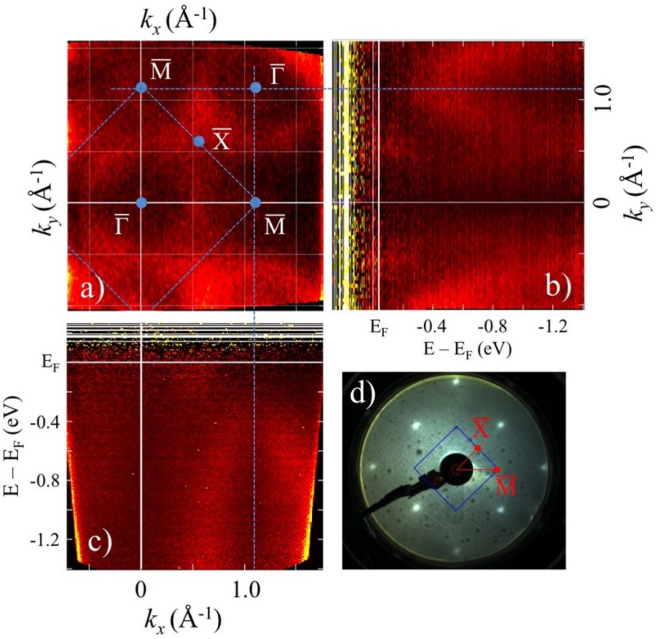

Figure 1. The ARPES results for a 6 u.c. (12.6 nm) thick $Sr_3Ir_2O_7(001)$ thin film, taken at room temperature, along with an isoenergy plot along both the k_x and k_y directions (001) plane, near the Fermi level (E_F). The experimental valence band electronic structure was taken with a photon energy of 71 eV. (a) The two-dimensional mapping of k_x and k_y, at $E - E_F = -0.2$ eV (-0.2 eV below E_F). (b) The dispersion along k_y for $k_x = 0$ line. (c) The dispersion along k_x for $k_y = 0$ line. (d) The LEED image taken with electron kinetic energy of 38.5 eV, with an overlay of the Brillouin zone and the high symmetry lines, $\overline{\Gamma X}$ and $\overline{\Gamma M}$.

3. The $Sr_3Ir_2O_7(001)$ Brillouin zone

Figures 1(a)–(c) shows the ARPES band mapping of a 6 u.c. (12.6 nm) thick $Sr_3Ir_2O_7(001)$ film just below the Fermi level (at $E - E_F = -0.2$ eV). The LEED patterns confirm that the surface lattice is well ordered and retains four-fold symmetry. The isoenergy cut (figure 1(b)) through $Sr_3Ir_2O_7(001)$ band structure was constructed from the ARPES experimental band structure plots along the k_y direction (figure 1(a)) and along the k_x direction (figure 1(c)). The $Sr_3Ir_2O_7(001)$ surface Brillouin zone can be reconciled with the LEED pattern only if the edge of the Brillouin zone ($\bar{X}$) is at 0.81 Å^{-1} and the corners of the square Brillouin zone ($\bar{M}$) are at 1.15 Å^{-1}.

The surface Brillouin zone can be definitively assigned from the extensive analysis of LEED results, as shown in figure 1(d), and the Brillouin zone critical points in the isoenergy cut of the band structure in figure 1(a). Just below the Fermi level (at $E - E_F = -0.2$ eV), the isoenergy cut through the $Sr_3Ir_2O_7(001)$ band structure (figure 1(a)) is in sharp contrast to that seen for bulk $Sr_3Ir_2O_7(001)$ single crystals at the top of the valence band [15, 16], as the observed thin film Brillouin zone here is much larger. The observed surface lattice constant is 3.9 ± 0.2 Å. A similar lattice constant of 3.9 Å, obtained via scanning tunneling microscopy, has been reported for the Sr–O surface termination of the bulk $Sr_3Ir_2O_7(001)$ single crystal [17]. This is also consistent with the in-plane lattice constant of the $(LaAlO_3)_{0.3}(Sr_2TaAlO_6)_{0.7}$ substrate of 3.87 Å. In contrast, an in-plane unit cell of 5.5 Å is expected of the bulk $Sr_3Ir_2O_7(001)$ single crystal due to the oxygen octahedral rotation [15–17]. This means that the expected lattice distortion of $Sr_3Ir_2O_7(001)$ single crystal is either lost in the thin film, or the Brillouin zone is dominated by the Sr–O termination.

For $Sr_3Ir_2O_7(001)$ thin films, there is a large density of states at the Fermi level in the vicinity of $\bar{X}$. This is clearly evident in a comparison of different isoenergy cuts across the band structure at the E_F (figure 2(a)), and with increasing binding energies below the E_F at $E - E_F = -0.1$ eV (figure 2(b)), at $E - E_F = -0.2$ eV (figure 2(c)), at $E - E_F = -0.3$ eV (figure 2(d)), at $E - E_F = -0.4$ eV (figure 2(e)), and at $E - E_F = -0.5$ eV. It is also clear that the symmetry of the Brillouin zone is preserved with increasing binding energy. Although the experimental band structure for the $Sr_3Ir_2O_7(001)$ thin films (figure 1), including the isoenergy cuts through the band structure (figure 2), are not as sharp as the experimental band structures for $Sr_3Ir_2O_7(001)$ single crystals [15, 16] obtained from ARPES, the basic features seen in the isoenergy cuts of the band structure near the E_F are very similar.

Although the LEED is very sharp (figure 1(d)), indicative of high crystalline order in the $Sr_3Ir_2O_7(001)$ thin films, especially at the surface, the angle resolved photoemission band structure does not exhibit the sharp and distinct bands obtained in the angle resolved experiments taken on cleaved surfaces for the $Sr_3Ir_2O_7(001)$ bulk single crystals [15, 16]. Figure 3 compares the isoenergy cuts taken on 4.2 nm (2 u.c.) thick and 13.6 nm (6.5 u.c.) thick $Sr_3Ir_2O_7(001)$ films taken just below the Fermi level, $E - E_F = 0.2$ eV. Not surprisingly, the band structure becomes more diffuse in the thinner films, as indicated in figures 3(a) and (c). This trend is also apparent in the band plots along the $\overline{\Gamma M}$ symmetry direction (k_x direction at $k_y = 0$) for the 13.6 nm (figure 3(b)), and 4.2 nm (figure 3(d)) thick films.

4. The finite density of states at the Fermi level for $Sr_3Ir_2O_7(001)$

As shown in the band dispersion in figure 4, the $Sr_3Ir_2O_7(001)$ thin films exhibit a finite density of states at the E_F, which is similar to that observed in the experimental band structure of $Sr_3Ir_2O_7(001)$ single crystals reported in [15]. For both the 13.6 nm (figure 4(c)) and 4.2 nm (figure 4(d)) thick $Sr_3Ir_2O_7(001)$ thin films, the spectral intensity is vastly enhanced if the integration is increased from a binding energy range of -0.1 to -0.2 eV (dashed blue area) to a binding energy range from E_F to -0.2 eV (dashed green area). These spectral intensity plots clearly indicate that there is a finite density of states near E_F. The absence of any strong photovoltaic charging in the XPS core level binding energies further support that the surface of these $Sr_3Ir_2O_7(001)$ thin films is fairly conducting [29–32].

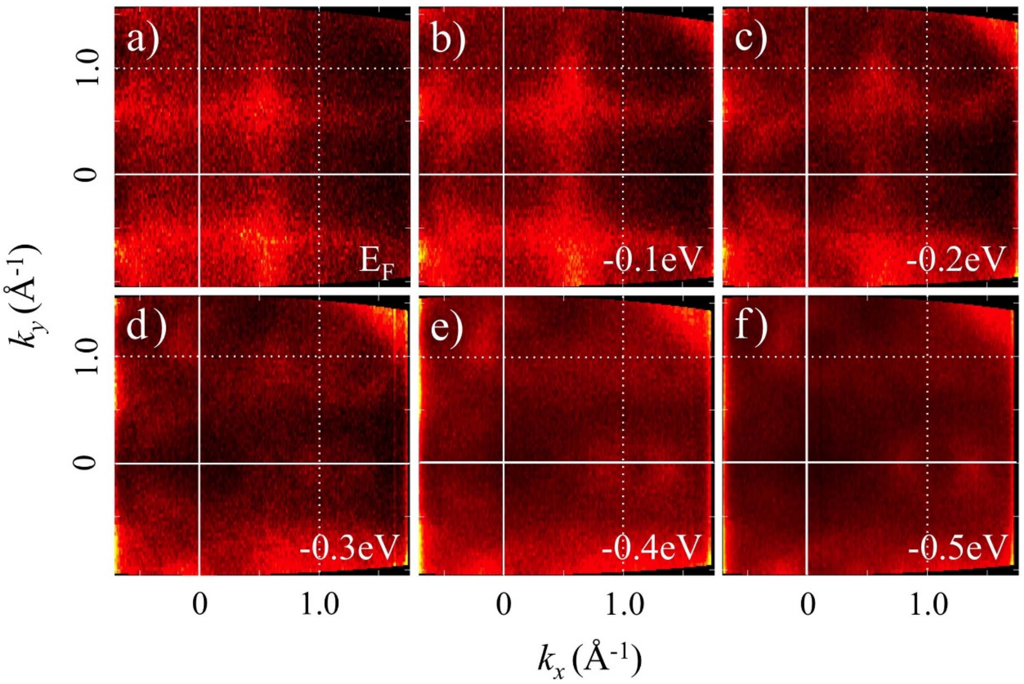

Figure 2. The isoenergy valence band 2D electronic structure mappings of a 6 u.c. (12.6 nm) thick $Sr_3Ir_2O_7(001)$ thin film as derived from ARPES measurements, plotted along both the k_x and k_y directions. The ARPES data was taken at room temperature with a photon energy of 71 eV. The isoenergy cuts are taken at binding energies (a) near E_F, and at (b) $E = -0.1$ eV, (c) $E = -0.2$ eV, (d) $E = -0.3$ eV, (e) $E = -0.4$ eV, and (f) $E = -0.5$ eV below E_F.

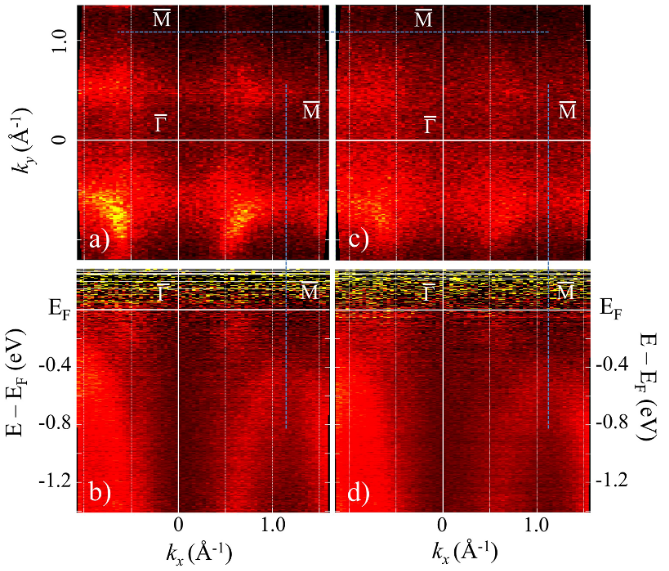

Figure 3. The experimental valence band electronic structure for (a), (b) 13.6 nm (6.5 u.c.) and (c), (d) 4.2 nm (2 u.c.) thick $Sr_3Ir_2O_7(001)$ films. (a) and (c) show the two-dimensional isoenergy band mapping, for in-plane k_x and k_y, at $E - E_F = -0.2$ eV (a) and just below E_F (c). (b) and (d) show the energy dispersion along $\overline{\Gamma M}$ symmetry direction, which is the k_x direction at $k_y = 0$, in (a) and (c). Data derived from angle-resolved photoemission, taken at room temperature, with a photon energy of 71 eV.

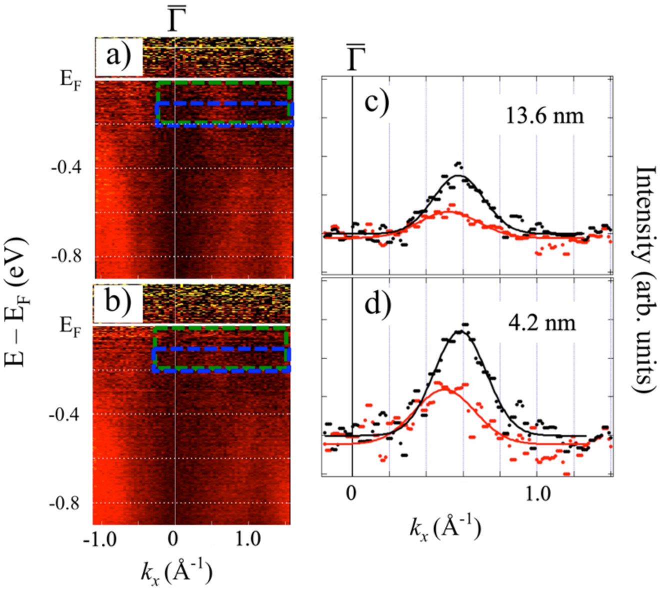

Figure 4. (a), (b) The band dispersion for the (a) 13.6 nm (6.5 u.c.) thick and (b) 4.2 nm (2 u.c.) thick $Sr_3Ir_2O_7$(001) thin films along the $\overline{\Gamma M}$ symmetry directions. (c), (d) The experimental integrated intensity as a function of wave vector along the $\overline{\Gamma M}$ symmetry direction, for (c) 13.6 nm thick and (d) 4.2 nm thick (red) $Sr_3Ir_2O_7$(001) thin films. The integration was done in the binding energy range of (c) -0.1 to -0.2 eV (denoted by the blue boxes) is plotted in red and the integration was done in the energy range from E_F to -0.2 eV (denoted by the dashed green area) is plotted in black.

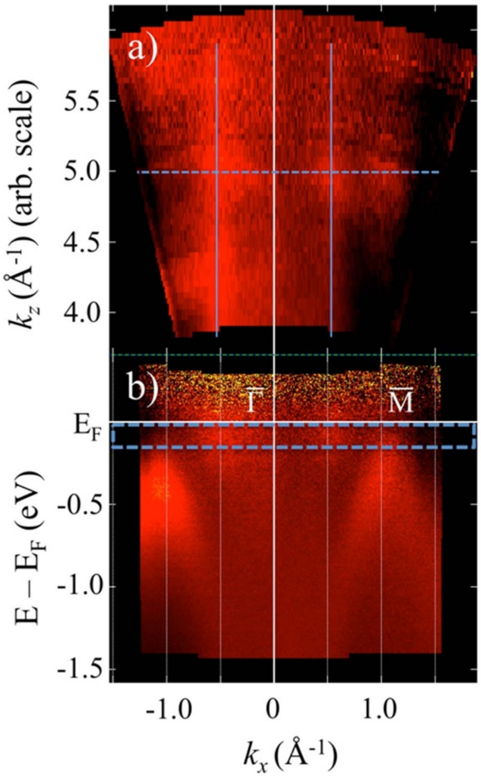

Figure 5. The photon energy dependence of ARPES for a 13.6 nm (6.5 u.c.) $Sr_3Ir_2O_7$(001) thin film surface. (a) The mapping for k_x, along the $\overline{\Gamma M}$ symmetry line and relative perpendicular wave vector k_z, corresponding to the density of states near E_F, as indicated in blue dashed rectangle area in (b). (b) The band mapping for k_x direction, along the $\overline{\Gamma M}$ symmetry line, corresponding to the $k_z \approx 5.0$, indicated in (a) by the horizontal dashed blue line. This horizontal line corresponds to a photon energy of 71 eV, within energy range of 50–132 eV investigated here.

Figure 5 shows the energy dependent ARPES spectroscopy for a 13.6 nm thick $Sr_3Ir_2O_7$(001) thin film. The bands contributing to the density of states at the E_F exhibit negligible dispersion along k_z, indicating a quasi-two-dimensional state, as seen in figure 5(a). The conservation of two-dimensionality of state suggests that the band that contributes to the density of states at the E_F are either surface states or surface resonances, i.e. localized electronic states at the surface. Thus, this photon energy dependent ARPES shows that the finite density of states at the E_F is highly localized to the surface region, confirming that is indeed a surface resonance and/or surface state.

The localized density of states near the Fermi level seen here is similar to what has been observed for bulk $Sr_3Ir_2O_7$(001) single crystals [15], where the states near E_F also showed little dispersion in wave vector perpendicular to the surface. In comparing the experimental band structure and density function theory, the bulk $Sr_3Ir_2O_7$(001) single crystal [15] appears p-type. Here, a comparison of the experimental band structure with density function theory [15] suggests the thin film surface is n-type. The conduction band minimum is pushed below the E_F and is thus partially occupied.

The results suggest that the surface resonance and/or surface state drives the surface conducting, as occurs for Sb_2Te_3, Bi_2Te_3 and Bi_2Se [33] and EuO [34, 35]. One question is whether the finite density of states at the surface is preserved in the thin film limit, which occurs for Bi_2Se_3 only because of band offsets, relative to the E_F, in the thin film limit [36, 37]. Here, for the $Sr_3Ir_2O_7$(001) thin films, the finite density of states does appear to persist to a film thickness of 2 u.c. (4.2 nm), as seen in figure 4.

The effect of the metallic or nearly metallic surface state becomes evident in the conduction of $Sr_3Ir_2O_7$(001) with decreasing film thickness. Figure 6 shows conductivity σ of $Sr_3Ir_2O_7$ as a function of film thickness at 100 K and 300 K. For the 11.8 nm thick and thicker films, σ is about 4×10^4 S m^{-1} at 300 K and shows only a weak thickness dependence. This conductivity is comparable with previous reports for epitaxial $Sr_3Ir_2O_7$ films [38, 39] and more than one order of magnitude higher than the bulk value [40]. The 4.2 nm (2 u.c.) film, surprisingly, exhibits a significantly higher conductivity σ of about 7×10^4 S m^{-1}. This is in sharp contrast to previous observations of correlated oxide thin films, which show suppressed conductivity with decreasing film thickness towards the electrical dead layer thickness [11, 13, 41–43]. All films exhibit insulating behavior, with lower σ at low temperatures. At 100 K, σ shows a similar film thickness dependence, with the conductivity increasing weakly from 1.1×10^4 S m^{-1} to 1.6×10^4 S m^{-1} as the film thickness decreases from 19.8 to 11.8 nm and then rises

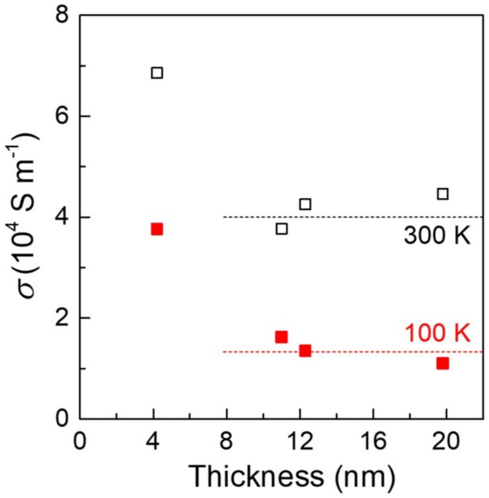

Figure 6. The conductivity σ as a function of film thickness at 100 and 300 K taken on 4.2–19.8 nm (2–9.5 u.c.) $Sr_3Ir_2O_7(001)$ films. The dashed lines serve as the guide to the eye.

sharply to 3.8×10^4 S m^{-1} in the 4.2 nm film. Notably, the thick films deposited on $(LaAlO_3)_{0.3}(Sr_2TaAlO_6)_{0.7}$ exhibits similar increasing conductivity with increasing temperature, characteristic of insulating behavior, to the thick films on $SrTiO_3$ [38, 39], suggesting that the substrate does not play a significant role in the emergence of metallicity in the ultrathin films. The enhanced conductivity in the thinner film suggests that the observed metallicity arises primarily from a surface effect: as the film becomes thinner, the contribution of the surface metallic state to the overall conduction becomes dominant, even though the bulk of the film remains insulating.

5. The comparison of $Sr_3Ir_2O_7(001)$ and $SrIrO_3(001)$

The Sr–O surface termination of $Sr_3Ir_2O_7(001)$, seen here and reported elsewhere [17, 44], is similar to the Sr–O surface termination of $SrIrO_3(001)$ [14]. Interestingly, the band structure, determined from ARPES for $Sr_3Ir_2O_7(001)$ thin films, also resembles the $SrIrO_3(001)$ band structure [14], as seen in figure 7. An expanded comparison of the $Sr_3Ir_2O_7(001)$ and $SrIrO_3(001)$ band structures with changing film thickness is shown in the supplementary materials (figure S4). A key difference between the experimental band structure of $Sr_3Ir_2O_7(001)$ thin films and the $SrIrO_3(001)$ band structure is that the top of the valence band for $Sr_3Ir_2O_7(001)$ is at about 0.58 Å^{-1}, while for $SrIrO_3(001)$ the top of the valence band is at 0.73 Å^{-1} along the $\overline{\Gamma M}$ high symmetry line of the surface Brillouin zone, seen in figure 7(d). This is distorted for $SrIrO_3(001)$, as the top of valance band is now shifted to 0.7 Å^{-1}, along the $\overline{\Gamma M}$ high symmetry line of the surface Brillouin zone, seen in figure 7(c). Unlike the insulating $Sr_3Ir_2O_7(001)$, the 5 nm (12.5 u.c.) thick $SrIrO_3(001)$ films are semimetals with close to fully compensated charges [13].

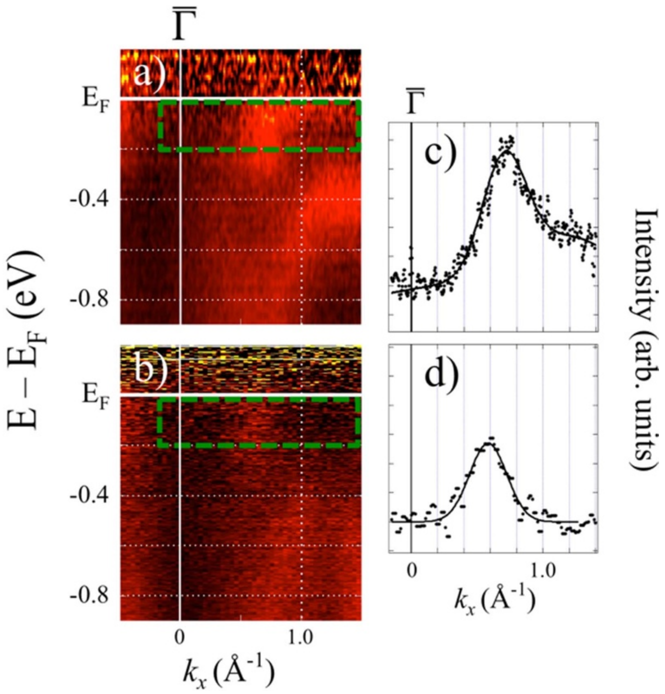

Figure 7. The comparison of the valence band electronic structures as a function of wave vector along the $\overline{\Gamma M}$ symmetry direction for (a) a 5 nm (12.5 u.c.) thick $SrIrO_3(001)$ thin film and (b) a 13.6 nm (6.5 u.c.) thick $Sr_3Ir_2O_7(001)$ thin film. Shown are the integrated density of state between E_F and 0.2 eV binding energy, indicated by dashed green, as a function of wave vector along the $\overline{\Gamma M}$ symmetry direction for both the (c) $SrIrO_3(001)$ and (d) $Sr_3Ir_2O_7(001)$ thin films.

6. Conclusions

We have investigated the electronic structure of the $Sr_3Ir_2O_7(001)$ thin films using ARPES spectroscopy. We have clear evidence of a finite density of states at the Fermi level that appears to be the result of a surface resonance and/or surface state. This density of states at the Fermi level may well persist into the thin film limit. The Brillouin zone for the $Sr_3Ir_2O_7(001)$ thin films is much larger than suggested for the bulk $Sr_3Ir_2O_7(001)$, although the mapped band structure at the Fermi level is very similar. The Brillouin zone critical points are consistent with the LEED results. The $Sr_3Ir_2O_7(001)$ thin films are terminated in Sr-O as seen for this and other iridates. The band structure of the $Sr_3Ir_2O_7(001)$ thin films are similar, but not identical, to the band structure for $SrIrO_3(001)$ iridate thin films.

Data availability statement

All data that support the findings of this study are included within the article (and any supplementary files).

Acknowledgments

This work was supported by the National Science Foundation (NSF) through the EPSCoR RII Track-1: Emergent Quantum

Materials and Technologies (EQUATE), Award No. OIA-2044049 and by the Nebraska Public Power District through the Nebraska Center for Energy Sciences Research at the University of Nebraska-Lincoln. The experiments were performed under the approval of HiSOR (Proposal No. 22AG020). The authors would like to thank Le Zhang for the growth of $SrIrO_3$(001) film and Prescott Evans for his assistance in acquiring the $SrIrO_3$(001) band structure data. The research was performed, in part, in the Nebraska Nanoscale Facility: National Nanotechnology Coordinated Infrastructure and the Nebraska Center for Materials and Nanoscience, which are supported by NSF under Award ECCS: 2025298, and the Nebraska Research Initiative.

ORCID iDs

Takashi Komesu https://orcid.org/0000-0002-2826-4193
Yuanyuan Zhang https://orcid.org/0009-0009-3711-7572
Shiv Kumar https://orcid.org/0000-0001-7793-9276
Kenya Shimada https://orcid.org/0000-0002-1945-2352
Peace Ikeoluwa Adegbite https://orcid.org/0009-0007-0781-2326
Xia Hong https://orcid.org/0000-0002-7873-5774
P A Dowben https://orcid.org/0000-0002-2198-4710

References

[1] Dhingra A, Komesu T, Kumar S, Shimada K, Zhang L, Hong X and Dowben P A 2021 Electronic band structure of iridates *Mater. Horiz.* **8** 2151–68

[2] Moon S J *et al* 2008 Dimensionality-controlled insulator-metal transition and correlated metallic state in 5d transition metal oxides $Sr_{n+1}Ir_nO_{3n+1}$ ($n = 1$, 2, and ∞) *Phys. Rev. Lett.* **101** 226402

[3] Cao G, Xin Y, Alexander C S, Crow J E, Schlottmann P, Crawford M K, Harlow R L and Marshall W 2002 Anomalous magnetic and transport behavior in the magnetic insulator $Sr_3Ir_2O_7$ *Phys. Rev.* B **66** 214412

[4] Zocco D A, Hamlin J J, White B D, Kim B J, Jeffries J R, Weir S T, Vohra Y K, Allen J W and Maple M B 2014 Persistent non-metallic behavior in Sr_2IrO_4 and $Sr_3Ir_2O_7$ at high pressures *J. Phys.: Condens. Matter* **26** 255603

[5] Zubko P, Gariglio S, Gabay M, Ghosez P and Triscone J M 2011 Interface physics in complex oxide heterostructures *Annu. Rev. Condens. Matter Phys.* **2** 141

[6] Hwang H Y, Iwasa Y, Kawasaki M, Keimer B, Nagaosa N and Tokura Y 2012 Emergent phenomena at oxide interfaces *Nat. Mater.* **11** 103

[7] Gariglio S, Caviglia A D, Triscone J M and Gabay M 2019 A spin-orbit playground: surfaces and interfaces of transition metal oxides *Rep. Prog. Phys.* **82** 012501

[8] Hao L, Meyers D, Dean M P M and Liu J 2019 Novel spin-orbit coupling driven emergent states in iridate-based heterostructures *J. Phys. Chem. Solids* **128** 39

[9] Zhang L, Pang B, Chen Y B and Chen Y 2018 Review of spin-orbit coupled semimetal $SrIrO_3$ in thin film form *Crit. Rev. Solid State Mater. Sci.* **43** 367

[10] Meyers D *et al* 2019 Magnetism in iridate heterostructures leveraged by structural distortions *Sci. Rep.* **9** 4263

[11] Groenendijk D J *et al* 2017 Spin-orbit semimetal $SrIrO_3$ in the two-dimensional limit *Phys. Rev. Lett.* **119** 256403

[12] Schutz P *et al* 2017 Dimensionality-driven metal-insulator transition in spin-orbit-coupled $SrIrO_3$ *Phys. Rev. Lett.* **119** 256404

[13] Zhang L, Jiang X, Xu X and Hong X 2020 Abrupt enhancement of spin-orbit scattering time in ultrathin semimetallic $SrIrO_3$ close to the metal-insulator transition *APL Mater.* **8** 051108

[14] Evans P E *et al* 2020 Decoupling the surface and bulk states in epitaxial orthorhombic $SrIrO_3$ thin films *AIP Adv.* **10** 045027

[15] Liu C *et al* 2014 Spin-correlated electronic state on the surface of a spin-orbit Mott system *Phys. Rev.* B **90** 045127

[16] Wang Q, Cao Y, Waugh J A, Park S R, Qi T F, Korneta O B, Cao G and Dessau D S 2013 Dimensionality-controlled Mott transition and correlation effects in single-layer and bilayer perovskite iridates *Phys. Rev.* B **87** 245109

[17] Okada Y *et al* 2013 Imaging the evolution of metallic states in a correlated iridate *Nat. Mater.* **12** 707–13

[18] Hogan T, Bjaalie L, Zhao L, Belvin C, Wang X, Van de Walle C G, Hsieh D and Wilson S D 2016 Structural investigation of the bilayer iridate $Sr_3Ir_2O_7$ *Phys. Rev.* B **93** 134110

[19] Subramanian M A, Crawford M K and Harlow R L 1994 Single crystal structure determination of double layered strontium iridium oxide [$Sr_3Ir_2O_7$] *Mater. Res. Bull.* **29** 645

[20] Matsuhata H, Nagaia I, Yoshida Y, Hara S, Ikeda S and Shirakawa N 2004 Crystal structure of $Sr_3Ir_2O_7$ investigated by transmission electron microscopy *J. Solid State Chem.* **177** 3776–83

[21] Martin R, Kim M, Lee C J, Mehar V, Albertin S, Hejral U, Merte L R, Lundgren E, Asthagiri A and Weaver J F 2020 High-resolution X-ray photoelectron spectroscopy of an IrO_2(110) film on Ir(100) *J. Phys. Chem. Lett.* **11** 7184–9

[22] Park Y J, Lee J, Park Y S, Yang J, Jang M J, Jeong J, Choe S, Lee J W, Kwon J D and Choi S M 2020 Electrodeposition of high-surface-area IrO_2 films on Ti felt as an efficient catalyst for the oxygen evolution reaction *Front. Chem.* **8** 593272

[23] Sarmin S *et al* 2020 Palm oil derived alkyd resin synthesis catalyzed by $SrO/Sr(OH)_2$ nanoparticles *J. Crit. Rev.* **7** 2131–9

[24] Karade S S, Sharma R, Gyergyek S, Morgen P and Andersen S M 2023 IrO_2/Ir composite nanoparticles (IrO_2@Ir) supported on TiN_xO_y coated TiN: efficient and robust oxygen evolution reaction catalyst for water electrolysis *ChemCatChem* **15** e202201470

[25] Grahmann C R, Pilleux M E and Fuenzalida V M 1994 Hydrothermal strontium titanate films on titanium: an XPS and AES depth-profiling study *J. Am. Ceram. Soc.* **77** 1601–4

[26] Nefedov V I 1982 A comparison of results of an ESCA study of nonconducting solids using spectrometers of different constructions *J. Electron Spectrosc. Relat. Phenom.* **25** 29–47

[27] Shimada K, Arita M, Takeda Y, Fujino H, Kobayashi K, Narimura T, Namatame H and Taniguchi M 2002 High-resolution, low-temperature photoemission spectroscopy at the HiSOR linear undulator beamline *Surf. Rev. Lett.* **9** 529

[28] Iwasawa H *et al* 2017 Rotatable high-resolution ARPES system for tunable linear-polarization geometry *Synchronton Radiat.* **24** 836

[29] Subedi A, Yang D, Yun Y, Xu X and Dowben P A 2024 Evidence for phase transitions in $CoFe_2O_4$ and $NiCo_2O_4$ thin films in temperature dependent x-ray photoelectron spectroscopy *J. Appl. Phys.* **57** 495301

[30] Baer D R, Artyushkova K, Cohen H, Easton C D, Engelhard M, Gengenbach T R, Greczynski G, Mack P,

Morgan D J and Roberts A 2020 XPS guide: charge neutralization and binding energy referencing for insulating samples *J Vac. Sci. Technol.* A **38** 031204

[31] Tasci T O, Atalar E, Demirok U K and Suzer S 2008 Electrical circuit modeling of surface structure for x-ray photoelectron spectroscopic measurements *Surf. Sci.* **602** 365–8

[32] Ertas G, Demirok U K, Atalar A and Suzer S 2005 X-ray photoelectron spectroscopy for resistance-capacitance measurements of surface structures *Appl. Phys. Lett.* **86** 183110

[33] Zhang H, Liu C-X, Qi X-L, Dai X, Fang Z and Zhang S-C 2009 Topological insulators in Bi_2Se_3, Bi_2Te_3 and Sb_2Te_3 with a single Dirac cone on the surface *Nat. Phys.* **5** 438–42

[34] Schiller R and Nolting W 2001 Prediction of a surface state and a related surface insulator-metal transition for the (100) surface of stochiometric EuO *Phys. Rev. Lett.* **86** 3847

[35] Sinjukow P and Nolting W 2003 Metal-insulator transition in EuO *Phys. Rev.* B **68** 125107

[36] Neupane M *et al* 2014 Observation of quantum-tunnelling-modulated spin texture in ultrathin topological insulator Bi_2Se_3 films *Nat. Commun.* **5** 3841

[37] Zhang Y *et al* 2010 Crossover of the three-dimensional topological insulator Bi_2Se_3 to the two-dimensional limit *Nat. Phys.* **6** 584–8

[38] Souri M, Terzic J, Johnson J M, Connell J G, Gruenewald J H, Thompson J, Brill J W, Hwang J, Cao G and Seo A 2018 Electronic and optical properties of La-doped $Sr_3Ir_2O_7$ epitaxial thin films *Phys. Rev. Mater.* **2** 024803

[39] Nishio K, Hwang H Y and Hikita Y 2016 Thermodynamic guiding principles in selective synthesis of strontium iridate Ruddlesden-Popper epitaxial films *APL Mater.* **4** 036102

[40] Li L, Kong P P, Qi T F, Jin C Q, Yuan S J, DeLong L E, Schlottmann P and Cao G 2013 Tuning the Jeff=1/2 insulating state via electron doping and pressure in the double-layered iridate $Sr_3Ir_2O_7$ *Phys. Rev.* B **87** 235127

[41] Hong X, Posadas A and Ahn C H 2005 Examining the screening limit of field effect devices via the metal-insulator transition *Appl. Phys. Lett.* **86** 142501

[42] Zhang L, Gardner H J, Chen X G, Singh V R and Hong X 2015 Strain induced modulation of the correlated transport in epitaxial $Sm_{0.5}Nd_{0.5}NiO_3$ thin films *J. Phys.: Condens. Matter* **27** 132201

[43] Hao Y, Chen X, Zhang L, Han M-G, Wang W, Fang Y-W, Chen H, Zhu Y and Hong X 2023 Record high room temperature resistance switching in ferroelectric-gated Mott transistors unlocked by interfacial charge engineering *Nat. Commun.* **14** 8247

[44] Adegbite P I, Subedi A, Zhang Y, Hong X, Komesu T and Dowben P A 2025 Anomalous behavior in the temperature-dependent low energy electron diffraction intensities for highly crystalline $Sr_3Ir_2O_7$ thin film surfaces *J. Phys.:Condens. Matter* **37** 165402